

Developing a Feasible Flap Control Design for Lifting Nano-ADEPT

Sarah N. D'Souza*, Wendy A. Okolo †, Ben E. Nikaido ‡, Bryan Yount §, Jason Tran ¶, Ben Margolis ||, Brandon P. Smith **, and Alan M. Cassell ††
NASA Ames Research Center, Moffett Field, CA, 94035

Breanna J. Johnson ‡‡
NASA Johnson Space Center, Houston, TX, 77058

Kenneth E. Hibbard §§, Jeffrey D. Barton ¶¶¶
John Hopkins University Applied Physics Laboratory, Laurel, MD

Zane Hays***
AMA, Inc., Moffett Field, CA, 94035

Precision landing of high mass payloads on Mars or returning sensitive samples from other planetary bodies to specific Earth locations are driving the development of an innovative NASA technology called a Deployable Entry Vehicle (DEV). DEV's have the potential to deliver a science payload with a stowed diameter 3-4 times smaller than an equivalent rigid aeroshell. NASA's Space Technology Mission Directorate (STMD) has successfully developed two types of DEVs, one that mechanically deploys and another that deploys via inflation. One of the current challenges in this domain is the design of advanced Guidance and Control (G&C) systems that enable a DEV to meet precision landing performance requirements. The primary design challenge is how to feasibly integrate a control system with a DEV since it has no back shell. To address this gap NASA's Space Technology Mission Directorate is currently funding a project at NASA Ames Research Center called Pterodactyl. This paper details the development of a flap G&C system for integration with a variant of a mechanical DEV called the Adaptable, Deployable, Entry, and Placement Technology (ADEPT) vehicle. This paper demonstrates the development of an eight flap, non-propulsive control system that: i) is statically stable in pitch and yaw, ii) is suitable for vehicle stabilization and steering, iii) utilizes an α/β guidance algorithm to precisely meet descent initiation target requirements, iv) consists of hardware that is readily made and/or obtained, and v) feasibly integrates with the vehicle's aeroshell deployment structure. This provides a solid foundation for optimizing a flap G&C system for DEVs.

I. Nomenclature

$$\begin{aligned} \alpha &= \text{angle of attack} \\ \beta &= \text{side slip angle} \end{aligned}$$

*Principal Investigator, Systems Analysis Office, NASA ARC/AA.

†Aerospace Research Engineer, Intelligent Systems Division, NASA ARC/TI.

‡Aerospace Flight Systems Engineer, Systems Analysis Office, NASA ARC/AA.

§Experimental Facility Developer, Engineering Systems Division, NASA ARC/RE.

¶Graduate Pathways Student, Systems Analysis Office, NASA ARC/AA.

||Graduate Pathways Student, Systems Analysis Office, NASA ARC/AA.

**Aerospace Flight Systems Engineer, Entry Systems & Vehicle Development Branch, NASA ARC/TSS.

††Aerospace Flight Systems Engineer, Entry Systems & Vehicle Development Branch, NASA ARC/TSS.

‡‡Aerospace Engineer, Flight Mechanics and Trajectory Design Branch, NASA JSC/EG5.

§§Principal Systems Engineer, Space Exploration Sector, JHU/APL

¶¶Guidance & Control Engineer, Force Projection Sector, JHU/APL.

***Research Assistant, Analytical Mechanics Associates, Inc.

δ	= flap deflection angle
γ	= flight path angle
λ	= longitude
Φ	= latitude
σ	= bank angle
ψ, θ, ϕ	= 3-2-1 euler angles between B and N frames (yaw, pitch, roll)
ξ	= heading angle
CoM	= center of mass
C_L	= lift coefficient
C_D	= drag coefficient
C_S	= side force coefficient
C_L	= rolling moment coefficient
C_M or CMy	= pitching moment coefficient
C_N	= yawing moment coefficient
CP	= pressure coefficient
I_{xx}	= moment of inertia with respect to the x-axis
I_{zz}	= moment of inertia with respect to the z-axis
$I_b^{B/B_{cm}}$	= inertia of the vehicle about its center of mass expressed in the body coordinates
L	= lift force [N]
\mathcal{L}, M, N	= body moments about $\hat{b}_x, \hat{b}_y, \hat{b}_z$
LE	= leading edge
Ma	= Mach number
TE	= trailing edge
$g[z]$	= force due to gravity, a function of z
\bar{q}	= dynamic pressure [bars]
m	= vehicle mass
p, q, r	= angular velocity between body and inertial frame about \hat{b}_x
z	= height/radial distance

II. Introduction

Precision landing of high mass payloads (≥ 2 metric tons [1]) on Mars or returning sensitive samples from other planetary bodies to specific Earth locations [2] are driving the development of an innovative NASA technology called a Deployable Entry Vehicle (DEV). A DEV, Fig. 1, enables a relatively large aeroshell to be stowed to a reduced diameter for launch and later deployed to provide a low-ballistic coefficient entry system. The stowing capability results in a significant relaxation of the vehicle size/landed mass constraints imposed by the available volume on current launch vehicles. For example, a DEV could deliver a science payload with a stowed diameter 3-4 times smaller than an equivalent rigid aeroshell (e.g. Stardust, Genesis, etc.) landing the same payload [2]. NASA's Space Technology Mission Directorate (STMD) has successfully developed two types of DEVs [3, 4]: i) Adaptable, Deployable, Entry Placement Technology (ADEPT) and ii) Hypersonic Inflatable Aerodynamic Decelerator (HIAD). Specifically, relevant thermal protection system (TPS) materials have been developed and manufactured to enable a flexible TPS for stowage. Additionally, the underlying deployment structures have been successfully integrated with the flexible TPS to demonstrate successful deployment of the TPS.

One of the current challenges in this domain is the design of advanced Guidance and Control (G&C) systems that enable a DEV to meet precision landing performance requirements. This is a critical capability for Mars landings and timely recovery of sample return missions to Earth. The current state-of-the-art for G&C is rooted in the precision Entry, Descent, and Landing (EDL) of rigid entry vehicles such as Mars Science Laboratory, Apollo and the Space Shuttle [5]. These entry vehicles use a Reaction Control System (RCS) to control the bank angle of the vehicle and consists of a set of small thrusters installed on the back shell (Fig. 2b). However, DEVs have no back shell, as illustrated in Fig. 3a. Revealing the primary design challenge for DEV G&C systems, how to feasibly integrate a control system with a vehicle that has no back shell.

STMD recognizes the need for this development and have supported a variety of feasibility studies through the Game Changing Development Program, as well as other externally funded efforts related to Entry, Descent, and Landing (EDL) technologies [6, 7]. Specifically, studies have examined the potential for using angle of attack and side slip (α/β ,

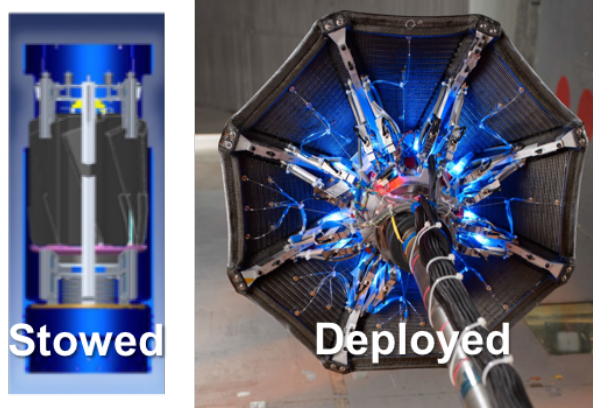


Fig. 1 Deployable Entry Vehicle Configurations

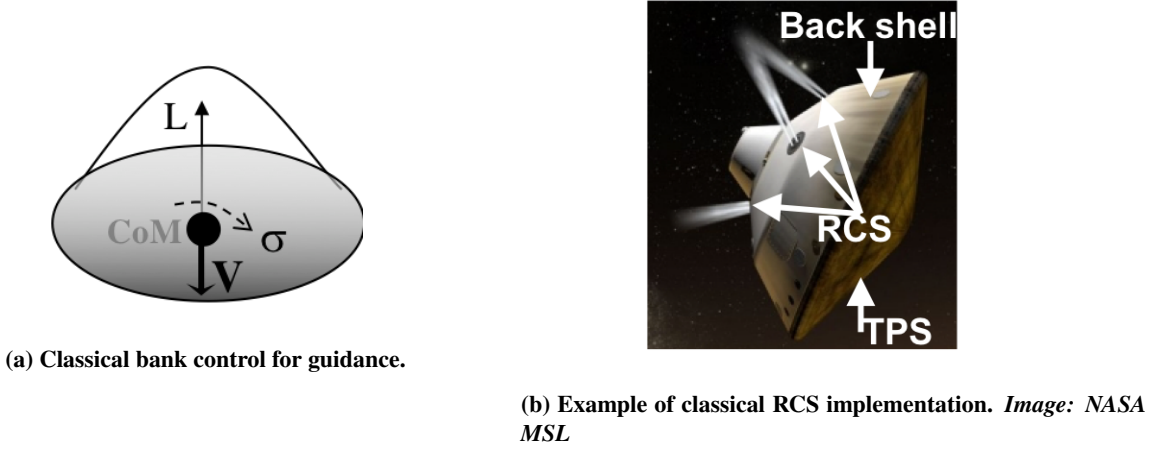


Fig. 2 Classical guidance and control method for rigid entry vehicles.

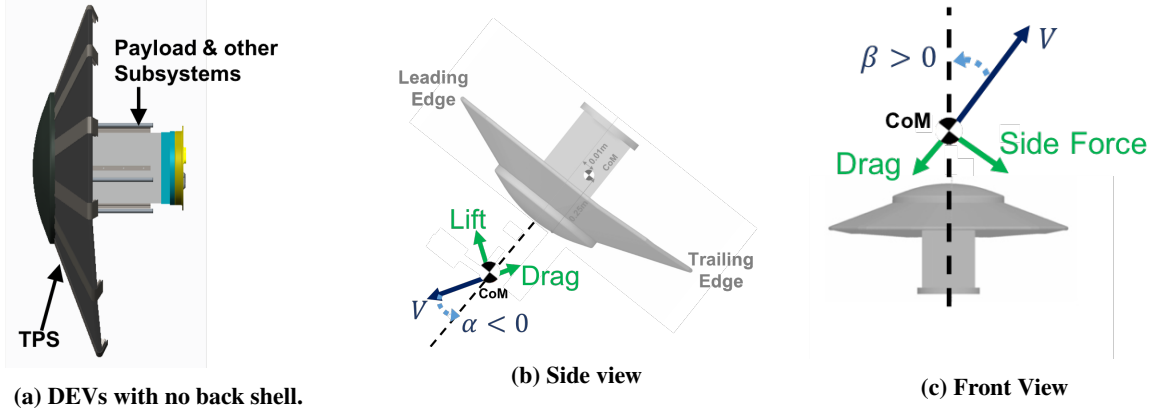


Fig. 3 DEV configuration and control variables.

Fig. 3b - 3c) control for guidance assuming the existence of a non-propulsive control system (e.g. shape morphing, flaps, etc) that can execute these guidance commands [8–10]. However, none of these studies have investigated the feasibility of these G&C systems in the context of hardware integration with DEV configurations.

To address this gap STMD is currently funding a project at NASA Ames Research Center called Pterodactyl.

Pterodactyl's primary goal is to develop a design, build and test capability for the feasible integration of G&C systems with DEVs. Pterodactyl will consider three different G&C configurations during the design phase: i) flaps for α/β control, ii) mass movement for α/β control, and iii) RCS for bank control. Each G&C configuration will be optimized using an Multi-Disciplinary, Design, Analysis, and Optimization (MDAO) framework developed by the Pterodactyl team. The optimized G&C configurations will then be traded against five specific figures of merit (FOMs): G&C system Performance, Programmatic Risk, Affordability and Life Cycle Costs, Extensibility and Flexibility, Safety and Mission Success. The objective of the design phase is to determine the best G&C system to build and test, since it would be cost prohibitive to build and test a prototype for each proposed G&C systems.

The MDAO framework will apply the concepts and tools developed for entry vehicle shape optimization [11, 12] to the optimization of G&C systems. The framework for Pterodactyl is illustrated in Fig. 4. The framework consists of four critical tools: i) Parametric Geometry and Mesh Generation, ii) Configuration Based Aerodynamics (CBAERO) with Anchoring, iii) JSC Flight Analysis and Simulation Tool with Monte Carlo, and iv) Mass Estimating Relationships (MERs). Tool descriptions can be found in the *Appendix: MDAO Tool Descriptions*. The design variables for the optimization are associated with the control system and will be explored to find the design that results in the smallest target foot print and minimum control system mass.

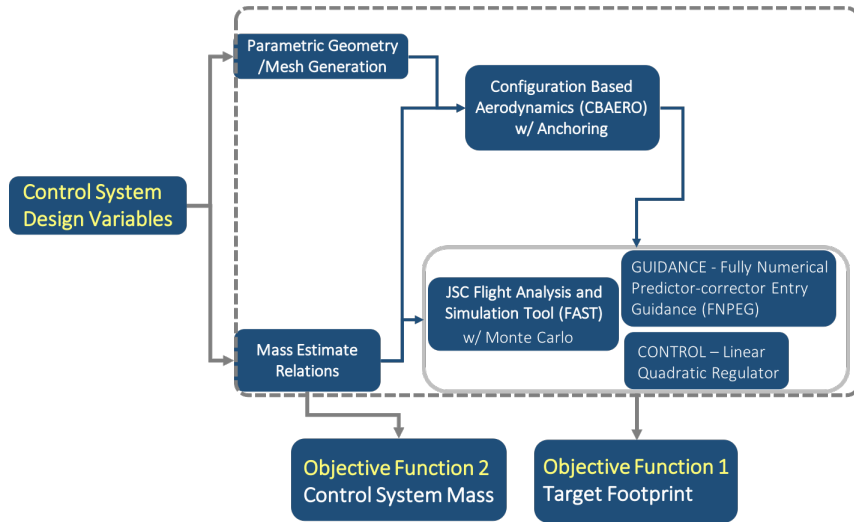


Fig. 4 MDAO Framework for Pterodactyl.

The development of this MDAO framework requires the integration of verified modeling and simulation tools and a feasible initial guess design for the optimization. Verified models and simulations guarantee that these tools will run successfully, for different designs, in the automated MDAO process. It is also critical that the initial guess for the design be part of a feasible design space for the given control system. This paper discusses the development of these tools and the initial guess design for flap control for α/β guidance.

III. Initial Design Development Overview

Pterodactyl is a technology demonstration and is not tied to a specific mission. Therefore, it is desired to select a mission that stresses the flap G&C system to find a feasible solution enabling flexibility across varied missions. Feasibility includes adequate targeting performance (target foot print < 5 km) and identification of control hardware that can be integrated with a DEV structure. Feasibility is determined through the development of specific simulations, including: CAD of the vehicle with primary subsystems, Computational Fluid Dynamics (CFD) for aerodynamic performance predictions, a guidance algorithm for α/β control, and stability & control analysis to identify the vehicle control authority. These simulations are discussed in Section IV. The following subsections discuss the assumptions, constraints, the baseline vehicle, and the nominal trajectory used in the development of the simulations required for initial design feasibility.

A. Assumptions and Constraints

The first and predominant constraint is that the aeroshell geometry & underlying substructures are fixed and cannot be fundamentally changed. This assumption ensures that the scope of this work remains on the G&C system feasibility and does not become an aeroshell shape study. Additionally, hardware integration feasibility is assessed with this constraint. The selected geometry is a variant of ADEPT ([13]) called Lifting Nano-ADEPT (LNA). This geometry was selected to leverage past work on LNA subsystem integration of avionics, deployment structures, and volume allocations for potential de-orbit, descent, and landing systems [7].

Next, it is assumed that this vehicle is performing an Earth re-entry after a mission to the Moon. A lunar return mission was selected because the high Earth entry speeds will stress the G&C design due to the need to manage high aerodynamics and heating loads. Demonstrating a feasible G&C system under these high loading conditions provides the potential to use this system multiple missions with similar or reduced loading conditions. Mars return velocities were not selected for this work because the scale of the vehicle would have to be increased to accommodate higher loading; violating the constraint that the aeroshell geometry is fixed.

A heat rate limit of 250 W/cm^2 was identified based on the ADEPT material limit determined through Arcjet testing at NASA Ames Research Center [2]. The g-load limit was determined to be 15 g's based on past missions and studies for returning non-biological or biological samples to Earth [14–19] that are sensitive to deceleration loads.

Finally, the scope of this G&C development is applied only to the entry phase of EDL operations. Additionally, Utah Test and Training Range (UTTR) was selected as the final target location of the because it is a common landing site for sample return entry vehicles. Note, however, that the entry phase terminates at the descent initiation point. Therefore, the G&C system will be designed to decelerate the vehicle from high entry speeds to a Mach number of 2 at a latitude and longitude corresponding to UTTR. The Mach = 2 condition was selected based on past studies [8] and missions that use a similar descent initiation point.

B. Baseline Vehicle and Subsystems

As mentioned above, the primary assumption for the DEV G&C design is that the aeroshell and associated subsystems are fixed. Pterodactyl has selected a variant of the ADEPT vehicle as the baseline fixed geometry. This vehicle was selected due to the significant amount of work completed to design and package the entry vehicle structure and required subsystems. ADEPT has two key features: i) a deployable rib structure and ii) a 3-D woven carbon fabric that is stretched over the rib structure to form the entry body aeroshell. The high temperature capability of the carbon fabric allows it to act as both the aeroshell structure and thermal protection system.

The Lifting Nano-ADEPT (LNA) variant of this entry system employs ribs of unequal lengths to form a raked-conic shape that generates lift. In Fig.5 the baseline LNA configuration with relevant subsystems is detailed. It has a one meter (39.4 in) nominal diameter, 70 degree cone angle, 12 ribs, and an open back aeroshell. Asymmetry for lift generation comes from longer ribs (and fabric) on what becomes the trailing edge side of the vehicle, as seen in Fig. 3b. The trailing edge side of the vehicle is approximately 16% longer than the rest of the vehicle. A volume equivalent to 12U cubesats (20cm x 20cm x 30cm) is provided for combined payload and vehicle subsystems. The result is an entry vehicle designed to deliver the equivalent of two cubesats of true payload. The baseline total entry mass is 59.4 kg before entry control systems are added. The LNA aeroshell and subsystems will not be allowed to change such that a total redesign of the integrated structure is required. This feasibility of integrating the flap control system hardware into the underlying rib structure, without a major redesign, will be assessed by the mechanical design team.

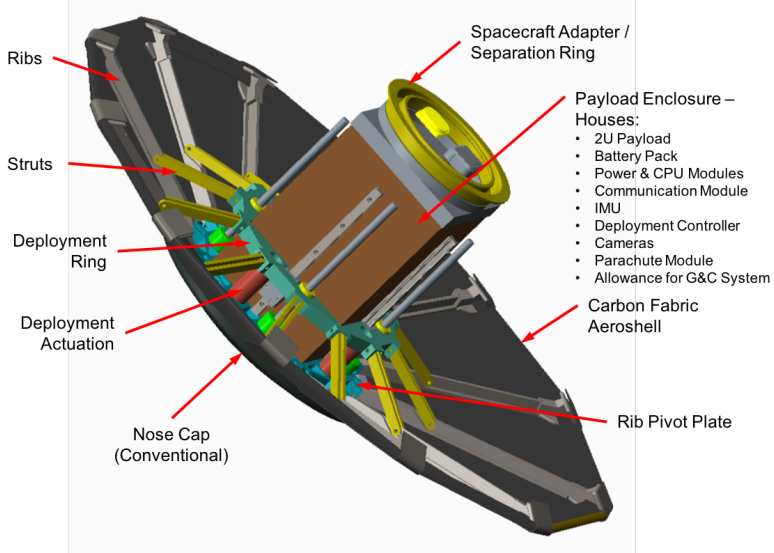


Fig. 5 Baseline LNA Configuration for Pterodactyl

C. Baseline Aerodynamics and Nominal Trajectory

Next, a nominal trajectory is needed to fully define the entry states and expected range of the entry trajectory. Identifying the nominal trajectory starts with finding the range capability provided by the LNA geometry. Several inputs are needed to determine of the LNA range capability: i) a feasible entry flight path angle (FPA) envelope, ii) an LNA aerodynamics database, and iii) a target location and energy. The target location and energy are known (Section III.A), but the entry FPA envelope and LNA aerodynamics must be defined. The process to find these values is iterative, however, for simplification, the final results for FPA and aerodynamics are discussed separately.

Entry FPA Envelope The entry FPA envelope was determined by running trajectories for three constant bank angles across a range of entry FPAs ($-10 \leq \gamma \leq -1$) with an entry altitude of 122 km and entry inertial velocity of 11 km/s. An estimate of the available lift to drag for LNA aerodynamics [7] were used as a first cut. Note that this methodology uses bank angle as a means to find the entry FPA envelope. Although we are using α/β control, using bank is a valid approach because the vehicle's performance will never exceed the capability of the maximum L/D condition, regardless of the guidance control variables.

Figures 6a and 6b plot the peak aerodynamic loading and peak heat rate experienced for each constant bank trajectory over the range of entry flight path angles (FPA). These figures show a dash-dot grey line that indicates the vehicle will skip out if the entry FPA is shallower than approximately -4 degrees. Also, note the heat rate and g-load limits identified by the dashed grey line in Figs. 6a and 6b, respectively. These boundaries are used to identify the valid region (green box) of possible entry FPA magnitudes. The valid region is identified to be between -5 degrees to avoid skip out and -6.5 degrees to stay below heating and g-load constraints. This set of entry FPAs also provide an indication of the range capability for this vehicle, as plotted in Fig. 7a. Taking a closer look, Fig. 7b shows that, for example, an entry FPA -5.5 degrees results in a range capability between 900 and 3400 km.

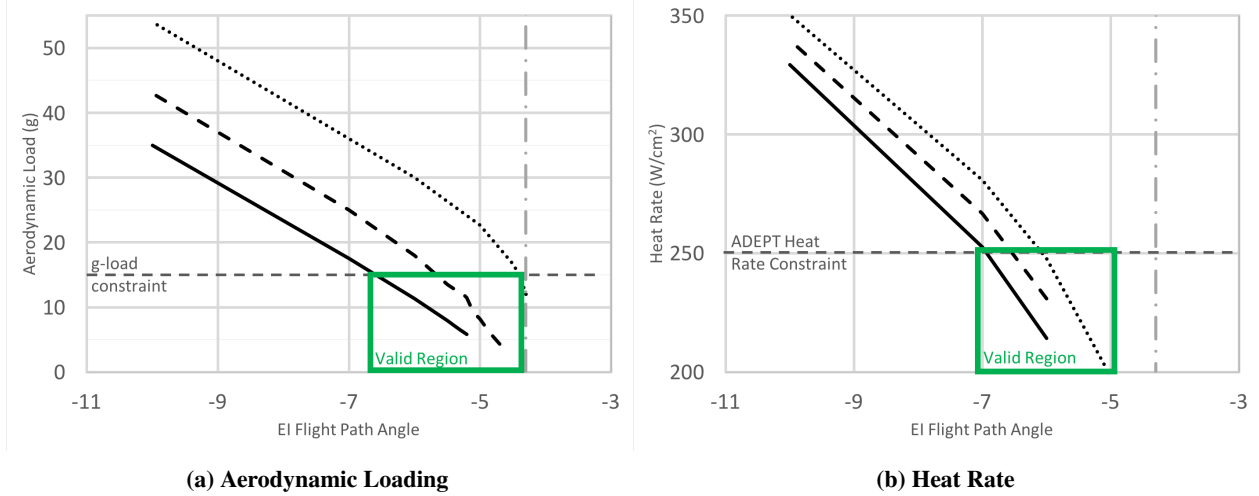


Fig. 6 Peak loads for Lunar return trajectories, unguided.

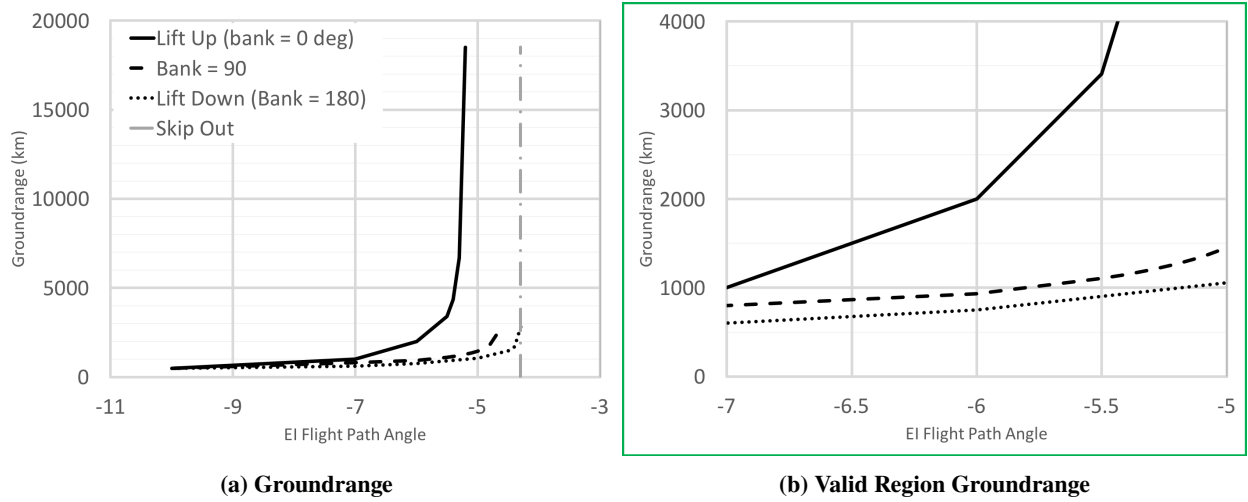


Fig. 7 Range capability for lunar return trajectories, unguided.

Baseline Aerodynamics The LNA aerodynamics include the force, $[C_L, C_D, C_S]$, and moment, $[C_L, C_M, C_N]$, coefficients which are generated using the LNA aeroshell geometry, flight conditions across possible trajectories, and vehicle attitude (α and β). The flight conditions, Mach number and dynamic pressure (\bar{q}), are a range of values defined from the the trajectories run in the entry FPA envelope analysis. The α and β ranges were selected not to exceed 20 and 10 degrees magnitude respectively. Payload shock impingement occurs beyond these attitude bounds of the flight envelope. The selected set of flight conditions and vehicle attitudes form the aerodynamic run matrix, which is found in Table 1. Using CBAero (see Appendix: Configuration Based Aerodynamics with Anchoring, MDAO Tool Descriptions)

Table 1 Aerodynamic run matrix for LNA.

Flight Conditions	Values
Ma	$[2, 5, 7.5, 10, 12.5, 15, 20, 25, 30, 40]$
\bar{q} [bars]	$[0.001, 0.005, 0.01, 0.015, 0.02, 0.025, 0.3, 0.5]$
α [deg]	$[0, -10, -15, -18, -20]$
β [deg]	$[-10 : 5 : 10]$

with the LNA geometry and the run matrix as inputs, initial estimates of the aerodynamic force and moment coefficients were determined. Figure 8 plots these coefficients versus Mach and dynamic pressure for one fixed angle of attack of -10 degrees and a sideslip angle of 10 degrees. The first row of Fig. 8 contains the lift (C_L), drag (C_D), and side force (C_S) coefficients (L-R) while the second row contains the roll (C_L), pitch (C_M), and yaw (C_N) moment coefficients (L-R). Fig. 8 shows that the coefficients are relatively independent of Ma and \bar{q} except for very low Mach and dynamic pressure regimes. Improving the prediction at Mach numbers less than 20 is discussed in Section VI: Future Work.

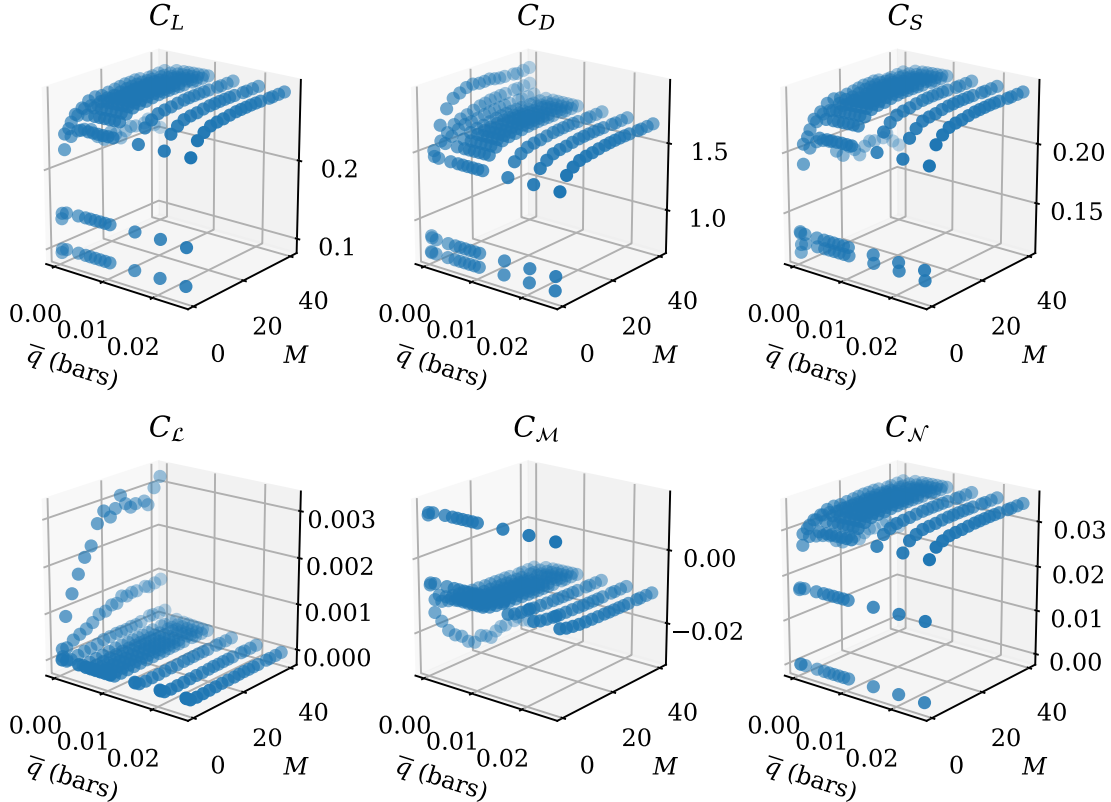


Fig. 8 Aerodynamic force and moment coefficients as a function of M and \bar{q} at $\alpha = -10$ degrees and $\beta = 10$ degrees.

Finally, Table 2 identifies the trim condition at four expected conditions the vehicle will fly through: i) entry guidance start at 0.5 g's, ii) maximum dynamic pressure, iii) Mach 20, and iv) descent initiation at Mach 2. Note that the trim conditions at $Ma \geq 20$ are independent of Mach number and the trim L/D is approximately 0.2 at an α of -12 degrees. However, the supersonic aerodynamics start to show dependence on Mach number, where a higher fidelity CFD code is required to capture the trim conditions at Mach = 2.

Table 2 Trim angle of attack and lift-to-drag ratio for LNA at specific flight conditions.

Key Trajectory Point	Flight Condition (Ma, \bar{q})	α_{trim} [deg]	L/D_{trim}
Entry Guidance Start	(40.1, 0.0022)	-12	0.2
Maximum Dynamic Pressure	(31.7, 0.0249)	-12	0.2
Mach = 20	(20.0, 0.006447)	-12	0.19
Descent Initiation, Mach = 2	(2.0, 0.01)	N/A	N/A

D. Nominal Trajectory

Using the entry FPA envelope, target location, target energy, and the baseline aerodynamics, a well defined guided nominal trajectory is designed. Note that unguided trajectories (constant bank with time) were used to define the entry FPA window. For a refined analysis of the nominal trajectory, guided trajectories (changing bank with time) for different entry FPAs within the valid region of the envelope are used. Specifically, NASA Johnson Space Center's Flight Analysis and Simulation Tool (FAST) with a Fully Numerical Predictor-corrector Entry Guidance (FNPEG, [20]) was used to determine these guided trajectories. FNPEG is used to design the trajectory such that the target would be reached at the desired energy of Mach 2 and an altitude of 30 km in order to meet the typical requirements for descent system initiation despite any aerodynamic or entry interface uncertainties. Additionally, the best entry FPA needs to be found so that i) it is not too steep such that the vehicle enters with an energy too high, thus exceeding load constraints (aerodynamic and heating) and ii) it is not too shallow such that the vehicle skips out of the atmosphere or significantly overshoot the target termination point. For these reasons, multiple trajectory ranges and flight path angles were studied to determine a smaller subset of acceptable, feasible ranges for LNA to fly. Figure 9b shows an example of feasible ranges for a flight path angle of -5.5 deg. Figures 9a - 9d demonstrate that as the distance to the target increases, FNPEG generates bank angle profiles that become increasingly lift up, where ϕ approaches zero, in order to extend the range capability of the vehicle and reach the target within 5 km. As shown in Figures 9e - 9f, this is achieved while abiding by the 250 W/cm^2 heat rate and 15 g aerodynamic load constraints.

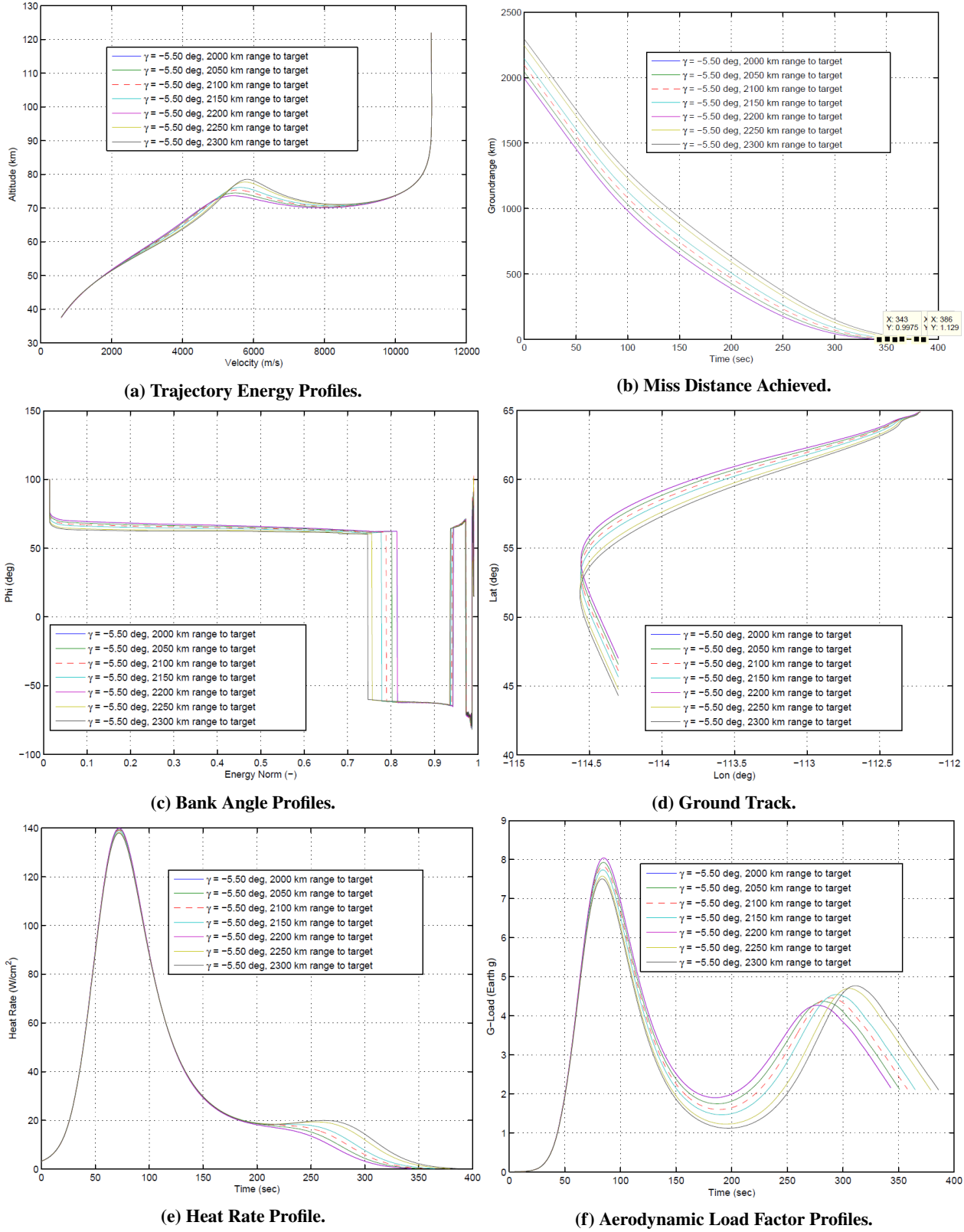


Fig. 9 FNPEG range sweep.

The inputs and targets defined in Tab. 3 are used to define the nominal guided trajectory which meets all heating, g-load, and target constraints.

Table 3 Entry State and Guidance Targets.

Entry Interface Parameters	Value	Units	FNPEG Target Parameters	Value	Units
Altitude	128	km	Altitude Target	6	km
Latitude	35	deg	Latitude Target	65	deg
Longitude	-114.2	deg	Longitude Target	-112.2	deg
Inertial Velocity	11	km/s	Velocity Target	0.69	km/s
Inertial Azimuth	0	deg			
Inertial Flight Path Angle	-5.5	deg			

Using the LNA aerodynamics and the entry & target states from Table 3 development of the initial design guess for flap control can be approached.

IV. Flap Control Configuration Design

The understanding of the LNA aeroshell and trajectory performance developed in the previous sections provide a foundation for finding a feasible solution for integrating a flap-type control system with LNA. As with any design process, the development of the this initial design was iterative. The Pterodactyl team looked at designs that included a six flap configuration and a minimum size flap configuration, however, it was found that these configurations did not provide enough control authority to track the $\alpha - \beta$ guidance commands. After some additional analysis, an eight flap configuration was sized for the maximum flap that could be packaged with the LNA structure as a secondary payload on the Aft Bulkhead Carrier (ABC) of a Centaur rocket (Fig. 10a). This launch vehicle and the ABC launch volume was selected as a reasonable initial starting point for this work. The maximum flap size and configuration was determined based on stowing constraints, volume limitations, and the potential control authority [10] for static trim tabs. The layout of the proposed control surface configuration is shown in Fig. 10b. There are four longitudinal tabs (two on the trailing edge and two on the leading edge of the LNA) for independent pitch control. Similarly, four lateral tabs numbered 3 to 6 in Fig. 10b, are designed primarily to generate yaw moments. Note the two flaps on the long ribs are smaller due to overall length constraints for packaging.

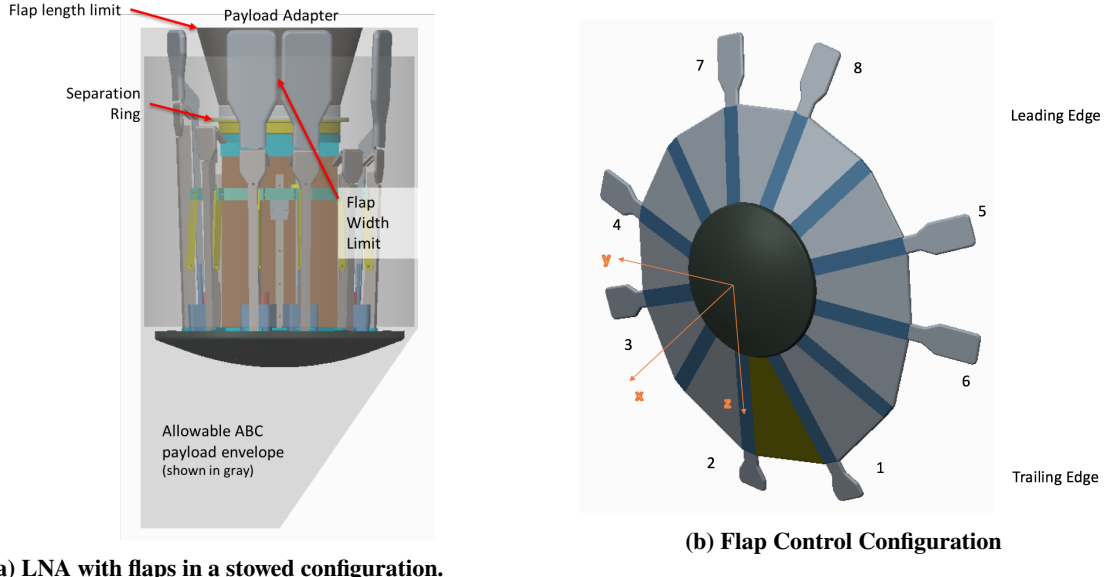


Fig. 10 LNA stowed and flap configuration.

The following subsections discuss the flap aerodynamics development, required flap control mechanisms, integration of these mechanisms with the LNA structure, the development of valid $\alpha - \beta$ guided trajectory, and stability and control analysis.

A. Flap Control Mechanisms and Integration

Recall that the LNA aeroshell and integrated subsystems are held fixed, allowing only incremental changes to the internal structure to allow for control system integration. The mechanical design team identified a feasible set of mechanisms such that incremental changes to the rib & rib tip structure are implemented without redesigning the full LNA aeroshell and subsystems. These changes resulted in several key design features, specific to the flap control system, which are highlighted in Fig. 11. First, the flaps are hinged about the centerline of the rib tip shoulder radius in order to ensure a smooth transition for the area exposed to the flow at entry. This results in a smooth geometry model that can be provided to CBAero for aerodynamics analysis. Second, the rib tips are slotted to allow for the insertion of the flap hinge, which differs from the rib tips that do not include flaps. Third, the hinged flaps are actuated via a motor driven slider-crank mechanism that enables flap rotations between 20 and -20 degrees. Fourth, each flap requires a motor drive unit which is installed within the payload enclosure. Finally, there is an additional mass allocation for flap control cable mass. These design features are present in eight of the twelve ribs which have flaps. The total mass for the LNA with flap control is 73.8 kg (including 15% mass growth allowance).

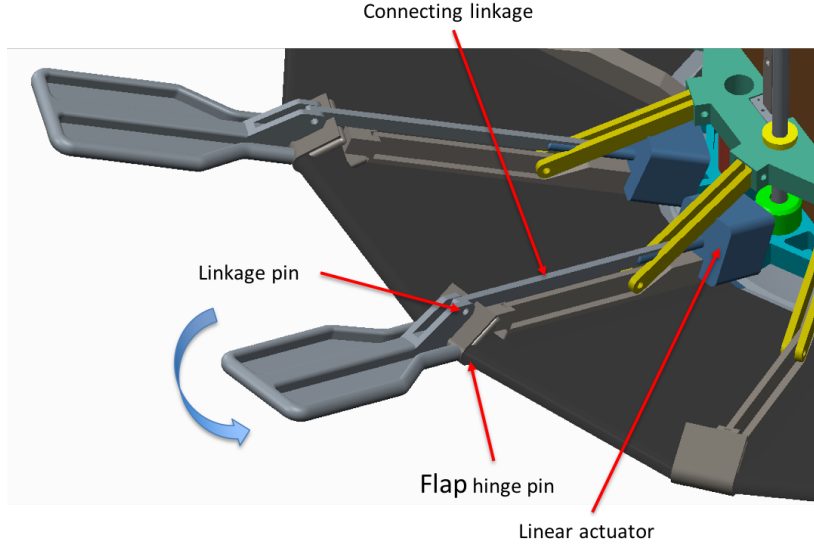


Fig. 11 Hinged flap mechanisms.

B. Flap Control Aerodynamics

Development of the LNA aerodynamics with flaps depends on the geometry selected to be run through CFD. Based on input from the aerodynamics, hardware integration and G&C teams, a geometry with a smooth attachment point between the flap and aeroshell was modeled. Next, with input from the teams, flap deflection angles were selected to range from -20 to 20 degrees. Figure 12 shows these flap deflections, where a zero degree deflection is parallel with the rib (dashed line), flap 1 is deflected 20 degrees into the flow, and flap 8 is deflected -20 degrees out of the flow.

In order for this aerodynamic data to be usable, the G&C teams need the incremental forces and moments for each flap, at discrete deflection angles. These increments are added to the LNA aeroshell aerodynamics (Eq. 1), depending on the set of flaps used to track the guidance commands, to get the total force and moment coefficients.

$$\begin{aligned} C_L &= C_{L,aeroshell} + \Delta C_{L,i=1:8} & C_D &= C_{D,aeroshell} + \Delta C_{D,i=1:8} & C_S &= C_{S,aeroshell} + \Delta C_{S,i=1:8} \\ C_{\mathcal{L}} &= C_{\mathcal{L},aeroshell} + \Delta C_{\mathcal{L},i=1:8} & C_M &= C_{M,aeroshell} + \Delta C_{M,i=1:8} & C_N &= C_{N,aeroshell} + \Delta C_{N,i=1:8} \end{aligned} \quad (1)$$

Therefore, each flap was run individually, at discrete deflection angles in 5 degree increments. For each deflected

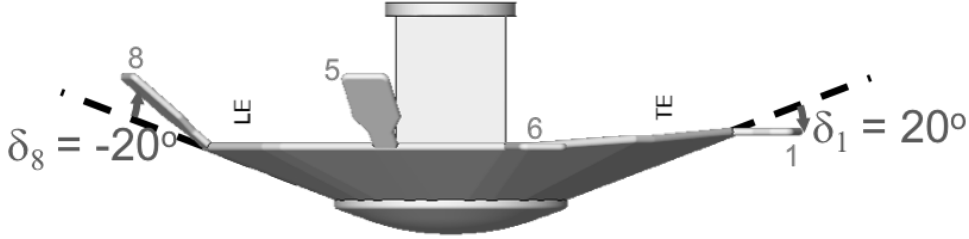


Fig. 12 Flap Deflection Angles Configuration

flap geometry the forces and moments were found at the conditions defined in the run matrix (Table 1). The following section will discuss the resultant static stability and control authority from these results.

C. Stability and Control Analysis

In this section, the static stability and controllability of the LNA, with and without flaps is analyzed from the LNA aerodynamic data. This is done to determine if the vehicle will return to its original steady-state configuration after being subjected to an atmospheric disturbance that slightly changes its orientation. In particular, the lateral stability needs to be characterized to determine the magnitudes of any roll-yaw coupling induced by a sideslip and identify instabilities, if any, exist. This will help to determine control requirements and assess whether stability augmentation, in addition to trajectory-tracking of guidance commands, will be required by the controller. It will also provide insight into the feasibility and challenges of achieving the alpha-beta guidance trajectory presented in Section IV.D, since the guidance commands for angle-of-attack and side-slip are generated independently.

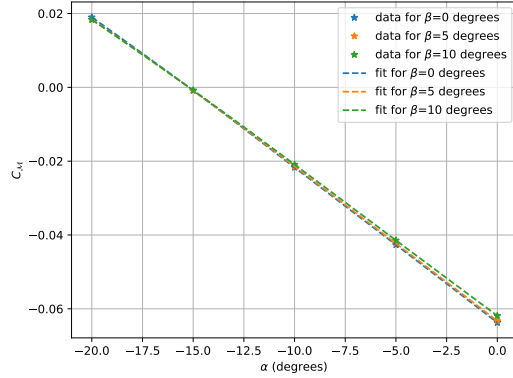
Aeroshell Moment Coefficients and Static Stability The static stability of LNA was evaluated by applying Multi-variable Adaptive Regression Splines [21] to curve fit the aerodynamic force and moment coefficients as a function of α , β , M , and \bar{q} . The use of regression splines is preferred because the functional expressions can be differentiated to directly obtain the static stability derivatives with their direct dependencies on α and β .

The stability derivatives of interest obtained from this data include the pitch stiffness derivative C_{M_α} , the dihedral derivative C_{L_β} , yaw stiffness C_{N_β} , and the coupled roll-yaw stability parameter $C_{N_{\beta,dynamic}}$. In Figs. 13a – 13c the original CBAero data as well as the interpolating splines for the relevant aerodynamic moment coefficients of interest are plotted. All coefficients depicted in Figs. 13a – 13c are at a fixed Mach number of 25 and dynamic pressure of 0.015 bars. This Mach and dynamic pressure condition is at a midpoint of the guidance trajectory shown in Section III.D. It is also representative of other trajectory conditions as Fig. 8 shows a relative independence of coefficients on Mach number and dynamic pressure.

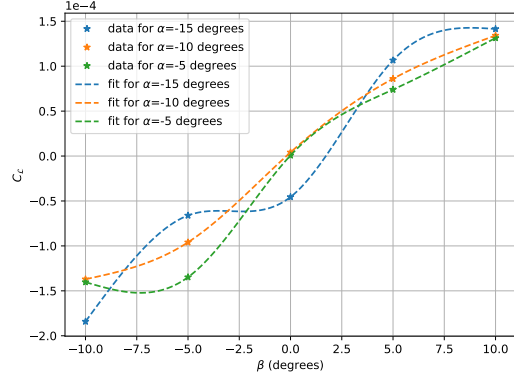
Fig. 13a shows the pitching moment coefficient (C_M) versus α for three sideslip angles: 0, 5 and 10 degrees. This coefficient is relatively independent of side slip and exhibits a linear dependency on angle of attack. Fig. 13b depicts the rolling moment coefficient (C_L) versus sideslip angle for three angle of attack values: -5, -10, and -15 degrees. The roll is two orders of magnitude smaller than both the pitch and yaw moment coefficients plotted in Figs. 13a and 13c, and is non-linear in β . In Fig. 13c, the yaw moment coefficient (C_L) variation is plotted with sideslip angle for three different angles of attack: -5, -10 and -15 degrees. Similar to the pitch moment case, the yaw moment coefficient is nearly linear with side slip and is relatively independent of angle of attack.

The spline interpolants of the aerodynamic force and moment coefficient data are differentiated with respect to the independent variables (angle of attack and sideslip). These expressions can be evaluated at different conditions to determine the stability of the vehicle. For presentation in this paper, the spline derivatives are evaluated at the same Mach number ($M = 25$) and dynamic pressure ($\bar{q} = 0.015$ bars) to show the static stability of the vehicle. The static stability coefficients of interest are the pitch stiffness C_{M_α} , the dihedral derivative C_{L_β} , and the yaw stiffness C_{N_β} , each defined as the derivative of the coefficient of the moment indicated by the first subscript with respect to the variable of the second subscript.

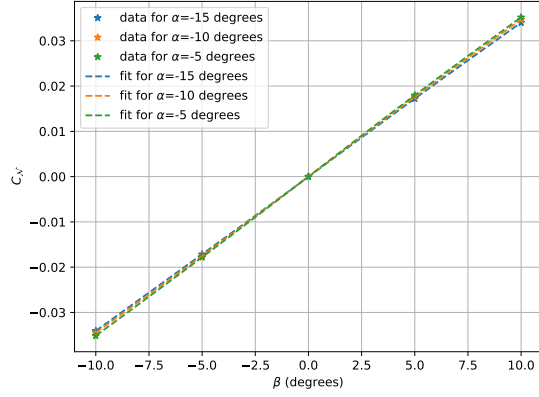
Fig. 14a shows the pitch stiffness, C_{M_α} , obtained from differentiating the spline inteprolant for C_M versus α shown in Fig. 13a at various sideslip angles. For longitudinal stability in pitch, this derivative should be negative and as seen in Fig. 13a, the LNA is statically stable in pitch. It is also observed that as the vehicle moves further away from the trim sideslip of zero, the pitch stability decreases slightly, with the overall conclusion remaining that the vehicle is



(a) Pitch moment coefficient C_M as a function of α for different β .



(b) Roll moment coefficient C_L as a function of β for different α .



(c) Yaw moment coefficient C_N as a function of β for different α .

Fig. 13 Moment coefficient trends with α and β for $Ma = 25$ and $\bar{q} = 0.015$ [bars].

longitudinally stable.

Figure 14b depicts the dihedral derivative $C_{L\beta}$, the slope of the rolling moment versus sideslip curve given in Fig. 13b. The $C_{L\beta}$ parameter should be negative to achieve positive stiffness in roll. As seen in the figure, the LNA is mostly unstable with negative stiffness in roll. As noted previously, the aerodynamic roll moment coefficient C_L is very small since the vehicle geometry is nearly axisymmetric. This also leads to very limited roll-yaw coupling as demonstrated by the small magnitudes of the $C_{L\beta}$ in Fig. 14b.

The yaw stiffness, the slope of the yawing moment curve due to sideslip seen in Fig. 13c, is plotted in Fig. 14c for different angles of attack. Fig. 14c shows that the LNA is stable in yaw as the $C_{N\beta}$ is positive for all angles of attack and sideslip. The $C_{N\beta,\text{dynamic}}$ derivative, a parameter that captures coupled lateral-directional stability at a given angle of attack, is given by Eq. 2. As the $C_{L\beta}$ is significantly smaller than its counterpart $C_{N\beta}$, the latter derivative dominates, resulting in a stable dynamic derivative as seen in Fig. 14d.

$$C_{N\beta,\text{dynamic}} = C_{N\beta} \cos \alpha - \frac{I_{zz}}{I_{xx}} C_{L\beta} \sin \alpha \quad (2)$$

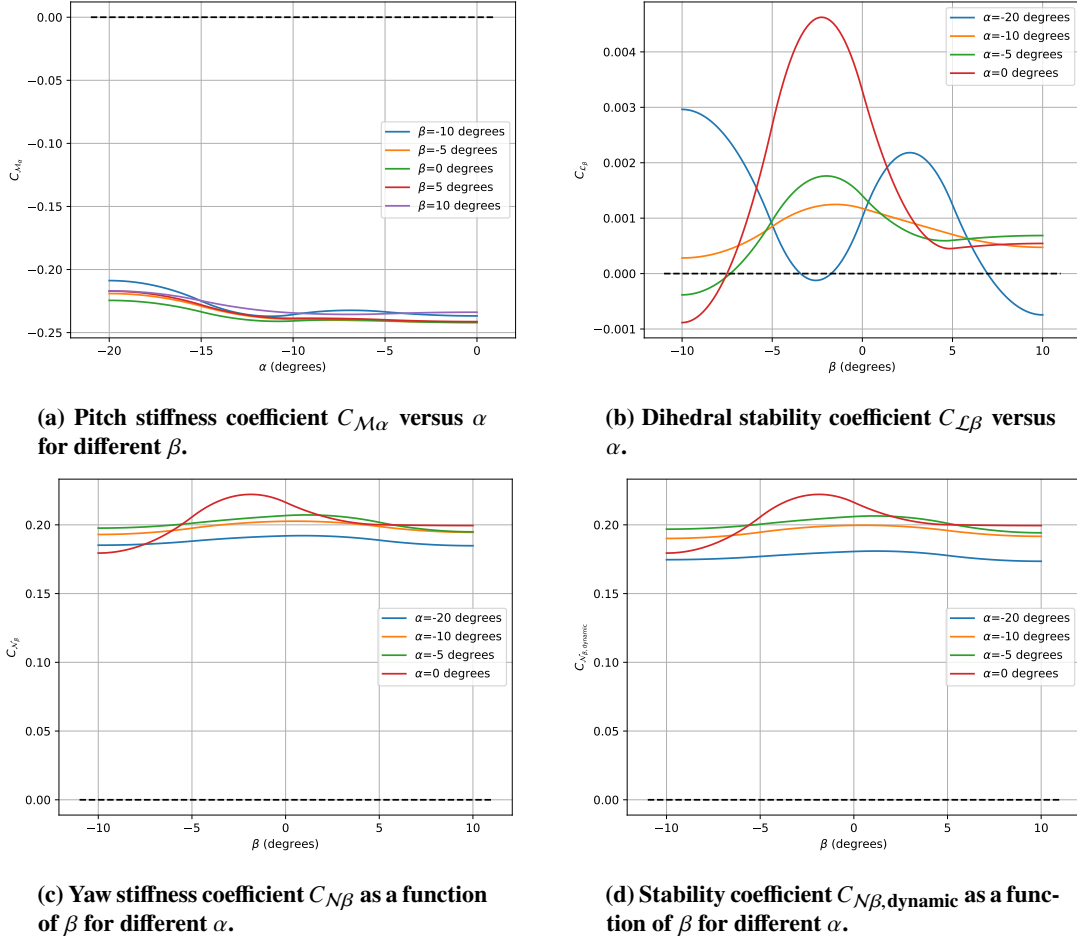


Fig. 14 Stability Derivatives.

Flap Control Authority Using the aerodynamic moments found for the flaps in Section IV.B, a subset of the aerodynamic moments are presented at the trim angle of attack and sideslip and the same Mach number and dynamic pressure points shown for the base aeroshell data in Fig. 13. For a single angle of attack, Mach number, sideslip angle, and dynamic pressure, the flaps are individually deflected from 20 degrees into the flow to -20 degrees out of the flow. This process is repeated for different points within the Mach and dynamic pressure operating regime of the vehicle, while varying sideslip and angle of attack. Fig. 15 shows the induced aerodynamic roll, pitch, and yaw moments (going from left to right) for deflections of control surfaces 7, 4, 3, and 2 (going from the top to the bottom). Since the vehicle is symmetric about the longitudinal x-z plane, only the tabs on one side of the vehicle are presented for brevity.

Fig. 15 shows that deflecting the longitudinal control surfaces 7 and 2 into the flow generates primarily positive and negative pitching moments respectively. These surfaces also generate secondary yaw moments as expected, when deflected individually into the flow and without their counterparts 8 and 1. Furthermore, they are also capable of generating roll moments of significantly smaller magnitudes as compared to the pitch or yaw. The lateral control surfaces 3 and 4 induce primarily yaw moments when deflected with secondary pitch moments generated. Furthermore, surfaces 3 and 4 can also create roll moments larger than their longitudinal counterparts 2 and 7 as expected. This induced roll is small in comparison to the primary yaw moments induced by deflecting the lateral tabs. The control surfaces can effectively induce pitch and yaw moments, making this control configuration suitable for tracking a guidance trajectory based on angle of attack and sideslip modulation.

Since the flap deflections move primarily inline with the roll axis of the vehicle, deflecting the tabs does not induce much roll except for the limited dihedral coupling that can also be seen in the base aeroshell, Fig. 14b. The base LNA was shown to be stable in pure pitch and pure yaw during the hypersonic regime of interest, but has an unstable dihedral

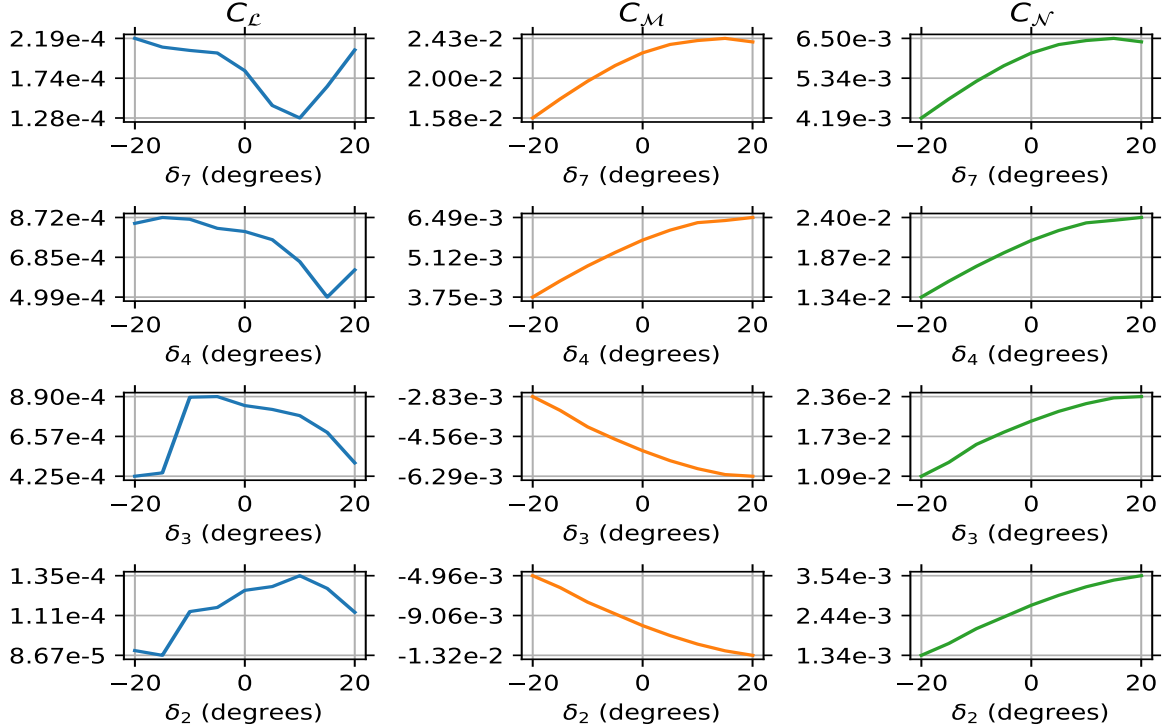


Fig. 15 Control Effector Authority: Aerodynamic Moments versus Surface Deflections

derivative. Thus, in addition to modulating the aerodynamic forces and moments to follow the guidance commands, the flaps will be used to stabilize the vehicle. Preliminary analysis shows that the flap configuration can be used for both stabilizing the vehicle and modulating α and β .

D. Developing an $\alpha - \beta$ Guidance Algorithm

The next step to making a flap configuration viable is to develop a guidance algorithm that provides $\alpha - \beta$ commands to control the longitudinal and lateral forces, respectively. Direct control of longitudinal and lateral directional forces has been explored as a possible entry guidance algorithm [9], but such a guidance has not been flown for lifting re-entry vehicles. A strong benefit of $\alpha - \beta$ guidance is the ability to control downrange and crossrange independently. Conversely, vehicles flown with bank-angle only guidance must rely on the vehicle's natural trim angle of attack, based on CG location at launch, to determine the magnitude of the lift vector to be steered with bank angle commands that reduce the total range to the target. The bank angle guidance must then determine when to change the sign of the bank angle magnitude and thus the direction of the lift vector to mitigate crossrange errors in a non-trivial fashion. Numbers of bank reversals and when to perform the reversals can easily become a great challenge for vehicles with low L/D, as bank reversals typically introduce errors into the predicted bank angle vs energy profile due to bank angle rate and acceleration limitations induced by the chosen control system. These factors, in addition to the aforementioned strengths of FNPEG, led to the decision to augment FNPEG, and create a new version of the numerical predictor corrector guidance, FNPEG with uncoupled range control (URC).

Similar to bank-angle FNPEG, FNPEG URC numerically minimizes a range to target cost function using the Newton-Raphson method and produces a commanded alpha and beta based on the vehicle's alpha and beta actuation capability range estimates. The linear angle of attack profile from the current energy state at each guidance time step to the user defined final energy state is computed to yield the new angle of attack command. A strong benefit of FNPEG, and now FNPEG URC, compared to other numerical predictor methods is the fact that this is a search for only one variable (bank or angle-of-attack) which helps improve the chance of convergence and the number of iterations needed to converge. Sideslip angle is determined by using a simplified Proportional Derivative control logic based on available crossrange capability and maximum expected sideslip control authority. Similar methodologies, from Section III.D, of determining a feasible subset of ranges and flight path angles were used to produce the trajectories in Figures 16a - 16d.

These plots demonstrate the feasibility of FNPEG URC to meet multiple ranges, from 2000 km to 2300 km, using the available L/D for an entry FPA of -5.5 degrees.

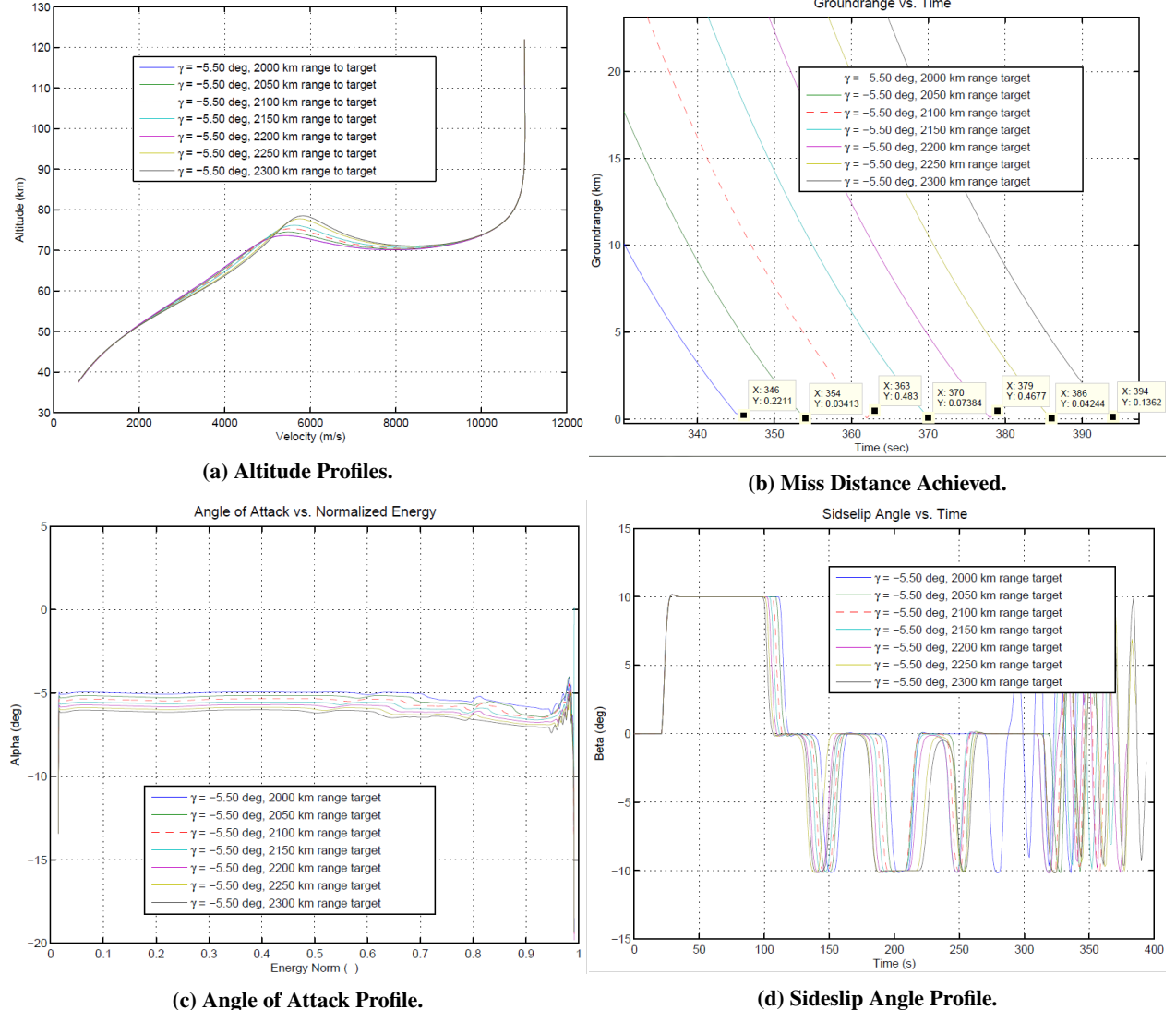


Fig. 16 FNPEG URC Range Sweep.

V. Conclusion

The work detailed in this paper provides the initial flap control system design to be explored in the MDAO framework. It was demonstrated that the eight flap, non-propulsive control system is statically stable in pitch and yaw, but unstable in roll. However, the predicted flap performance indicates that this flap configuration can be used to stabilize the vehicle and track guidance commands. Additionally, it was demonstrated that an α/β guidance algorithm successfully guides the vehicle precisely to the desired target point. Finally, a critical element of this research was demonstrated, that the hardware for a flap control system readily made and/or obtained and can feasibly integrated with the vehicle's aeroshell deployment structure. These results establish an understanding of the vehicle performance and hardware integration that is important to successfully optimizing this system. However, there is critical future work that the Pterodactyl team will be addressing and is discussed in the following section.

VI. Future Work

A. Structural and Thermal Protection System (TPS) Modeling

A critical part of future work is an understanding of the structural mass required to handle the high aerodynamic loading. Additionally, an understanding of the TPS material and thickness needed to handle the high heat rate and heat loads associated with the guided entry profile is needed.

MSC Nastran will be used to ensure positive margins of safety for potential structural failure modes by various load cases from the life cycle of the flap control system. The load cases will be maximum pressure on the flap during maximum dynamic pressure, maximum inertial deceleration loads, launch vehicle inertial loads, and thermal stresses at design temperature. For the component shown in Fig. 17, only the flap, crank-bracket, linkage bar, and pin structures will be analyzed while the ribs and rib tips are assumed rigid. Instead of relying on the use of nonlinear contact analysis, all load cases will be modeled in quasi-static equilibrium with reaction loads between the linkage-pin/crank-bracket and crank-bracket-pin/rib tip input as cosine bearing pressure loads. The quasi-static model is then solved for using Nastran's linear static solution procedure with inertia relief. The failure modes to be analyzed will include yield failure, ultimate failure, ultimate shear failure of pins, bearing yield failure, large deflection of trim tabs, and buckling of linkage bar. Margins of safety will then be calculated with factors of safety which satisfy NASA protoflight structure standards [22].

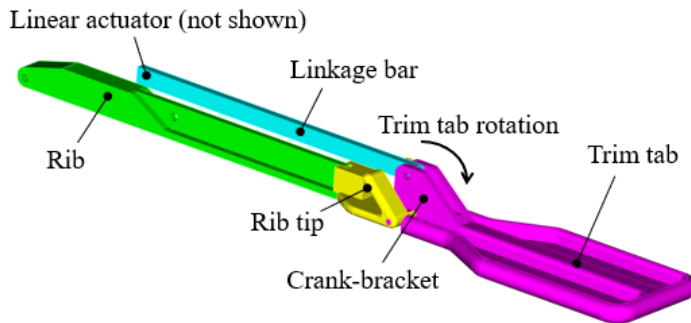


Fig. 17 Components of trim tab control system

TPSSizer and FIAT will be used to determine the amount of TPS mass required to protect the tabs from the heating predicted by CFD-based aeroheating analysis. Design driving points such as the maximum expected heat fluxes, heat loads, pressures, and recession will be used to select viable TPS material stack ups. Candidate TPS materials [23] which will be considered are C-PICA, HEEET, TUFROC, reinforced carbon-carbon, and carbon-phenolic. Because the flaps will not be in use during the entire trajectory, the aerothermal environment of the flaps are expected to have high heat fluxes but manageable heat loads. During the times when the tabs are not in use, they are stowed back and radiatively cool.

The models discussed here are under continued development to ensure that appropriate mass estimates for the structure and TPS are determined.

B. Improved Aerodynamic Estimates

As mentioned in this paper, higher fidelity CFD codes are required to improve the aerodynamic estimates for Mach numbers less than 20. A preliminary look at the aerodynamics using Equilibrium Cart 3D (see Appendix) was completed and compared to the CBAero results. Table 4 shows that for the same flight conditions that the vehicle flies through, the trim L/D is increased to 0.25 at an $\alpha_{trim} = -15^\circ$. Also, Cart 3D was able to capture the relevant aerodynamics at Mach = 2.

The force and moments coefficients are a direct function of the predicted pressure coefficients from the CFD code. Thus, the difference between the CBAero and Cart3D results comes from the pressures predicted from each code. Figure 18 shows the difference in pressure coefficient predictions on the LNA aeroshell for a Mach number of 3. Note how Cart 3D captures non-linear effects not captured by CBAero.

This is also depicted in Fig. 19 which illustrates the difference in predicted pressure (left) between CBAero and Cart3D for forward-deflected control surfaces and the resulting pitching moments (right). Note the high pressure regions

Table 4 Trim angle of attack and lift-to-drag ratio from Cart 3D for LNA at specific flight conditions.

Key Trajectory Point	Flight Condition (Ma, \bar{q})	α_{trim} [deg]	L/D_{trim}
Entry Guidance Start	(40.1, 0.0022)	-15	0.24
Maximum Dynamic Pressure	(31.7, 0.0249)	-15.05	0.25
Mach = 20	(20.0, 0.006447)	-15.075	0.25
Descent Initiation, Mach = 2	(2.0, 0.01)	-21	0.37

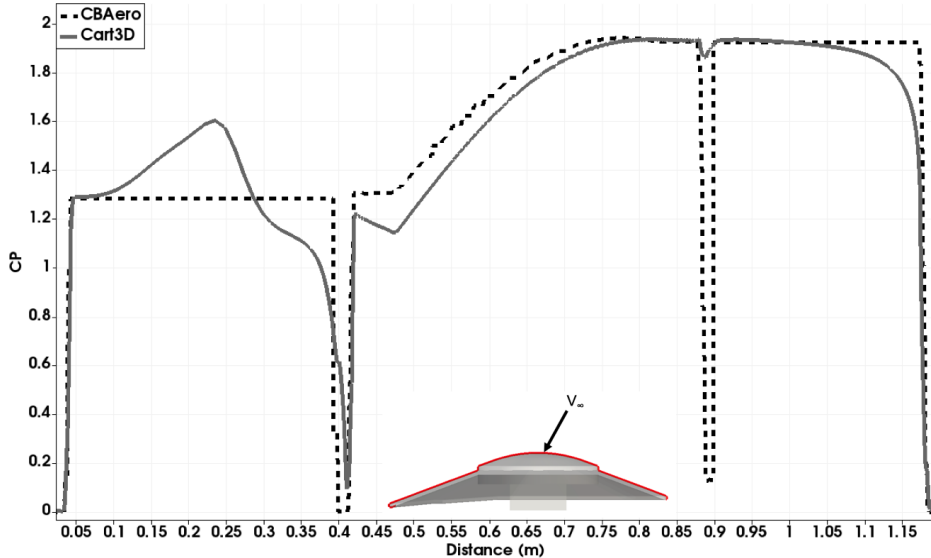


Fig. 18 Pressure Coefficient comparisons between CBAero and Cart3D for Mach 3, maximum dynamic pressure, at $\alpha = 15^\circ$.

(red) that are not captured by CBAero. Also note that the pitching moment coefficient is under predicted, for $\alpha < 0^\circ$, by CBAero. Increased fidelity of the moment coefficients is critical to the G&C systems design and is the focus of future work.

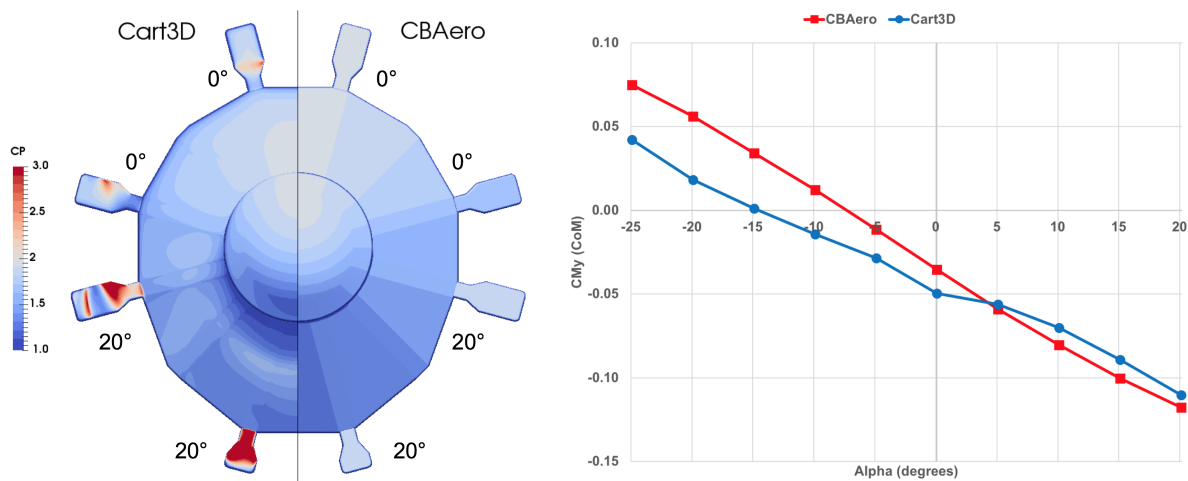


Fig. 19 Pressure and moment difference between CBAero and Cart3D. Mach 31.7, $q = 0.025$ bar

C. Guidance Development

The next step for guidance development will be to complete a Monte Carlo analysis to ensure that the final range chosen for the nominal trajectory has the strongest tolerance to dispersions and uncertainties, with each trajectory abiding by mission constraints. Once these ranges are chosen, another Monte Carlo analysis will be run on FNPEG URC nominal trajectories in order to determine the lowest alpha-beta rates and accelerations needed to still meet mission constraints and desired targeting performance. This is important because these minimum rates and accelerations are used by the controls team to determine the estimated minimum size/number of aerodynamic surfaces needed to achieve that desired targeting performance.

D. Control Methodology

The establishment of static stability and controllability allows for the development of the controller to track the $\alpha - \beta$ commands. Future work includes the development of a linear quadratic regulator (LQR) to achieve the guidance requirements along the trajectories described in Section IV.D. An LQR control algorithm was selected because it is robust to parameter uncertainties in the modeling such as aerodynamic dispersions and inaccuracies. In addition, both trajectory tracking and stabilization can be achieved for a controllable system with LQR.

A Multi-Input Multi-Output (MIMO) state-feedback integral controller is being developed using optimal control techniques to track guidance commands. The control variables to be calculated by the controller are the deflections of the eight aerodynamic control surfaces that track the angle of attack and sideslip commands. Equation 3 defines the system state.

$$x(t) = [V(t) \ \beta(t) \ \alpha(t) \ \sigma(t) \ p(t) \ q(t) \ r(t) \ \gamma(t) \ \xi(t) \ z(t)]^T \quad (3)$$

where $V(t)$ is the velocity of the vehicle, $\beta(t)$ and $\alpha(t)$ are the side-slip and angle of attack as before, $\sigma(t)$ is the bank angle, $p(t)$, $q(t)$, and $r(t)$ are the angular velocities between the body and inertial frames about body-fixed axes, $\gamma(t)$ is the flight path angle, $\xi(t)$ is the heading, and $z(t)$ is the altitude.

The control input vector is:

$$u(t) = [\delta_1 \cdots \delta_8]^T \quad (4)$$

where $\delta_1, \dots, \delta_8$ are the deflection angles of the 8 control surfaces.

The linear dynamics ignoring planet rotation (and latitude for heading rate) are given by

$$\begin{aligned} \dot{V}(t) &= -\frac{g[z(t)]}{m} \sin[\gamma(t)] - \frac{1}{m} D(t) \\ \dot{\gamma}(t) &= \left(-\frac{g[z(t)]}{m V(t)} + \frac{V(t)}{z(t)} \right) \cos[\gamma(t)] + \frac{1}{m V(t)} (L(t) \cos[\sigma(t)] - S(t) \sin[\sigma(t)]) \\ \dot{\xi}(t) &= \frac{1}{m V(t) \cos[\gamma(t)]} (L(t) \sin[\sigma(t)] + S(t) \cos[\sigma(t)]) \end{aligned} \quad (5)$$

where $L(t)$, $D(t)$, and $S(t)$ are the aerodynamic lift, drag, and side forces, respectively, and $g[z(t)]$ is the force due to gravity, dependent on altitude.

The rotational dynamics equations are

$$\begin{bmatrix} \dot{p}(t) \\ \dot{q}(t) \\ \dot{r}(t) \end{bmatrix} = \left(\mathbb{I}_b^{B/B_{cm}} \right)^{-1} \left(\begin{bmatrix} \mathcal{L}(t) \\ \mathcal{M}(t) \\ \mathcal{N}(t) \end{bmatrix} + \begin{bmatrix} p(t) \\ q(t) \\ r(t) \end{bmatrix}^T \mathbb{I}_b^{B/B_{cm}} \begin{bmatrix} p(t) \\ q(t) \\ r(t) \end{bmatrix} \right) \quad (6)$$

where $\mathbb{I}_b^{B/B_{cm}}$ is the inertia of the vehicle about its center of mass expressed in the body coordinates and $\mathcal{L}(t)$, $\mathcal{M}(t)$, and $\mathcal{N}(t)$ are the aerodynamic roll, pitch, and yaw forces, respectively.

The angular kinematics are defined by

$$\begin{aligned} \dot{\alpha}(t) &= -p(t) \cos[\alpha(t)] \tan[\beta(t)] + q(t) - r(t) \sin[\alpha(t)] \tan[\beta(t)] \\ \dot{\beta}(t) &= p(t) \sin[\alpha(t)] - r(t) \cos[\alpha(t)] \\ \dot{\sigma}(t) &= p(t) \cos[\alpha(t)] \sec[\beta(t)] + r(t) \sin[\alpha(t)] \sec[\beta(t)] \end{aligned} \quad (7)$$

and the altitude derivative is

$$\dot{z}(t) = V(t) \sin [\gamma(t)] \quad (8)$$

Here we formulate the time-varying finite-horizon LQR controller [24] which approximately minimizes the performance index

$$\int_{t_0}^{t_f} [\mathbf{x}(t) - \mathbf{x}^*(t)]^T Q [\mathbf{x}(t) - \mathbf{x}^*(t)] + [\mathbf{u}(t) - \mathbf{u}^*(t)]^T R [\mathbf{u}(t) - \mathbf{u}^*(t)] dt, \quad (9)$$

where the P and Q are constant weighting matrices. The system dynamics are linearized around the reference state and input trajectories, $\mathbf{x}^*(t)$ and $\mathbf{u}^*(t)$, defined as

$$\begin{aligned} A(t) &= \frac{\partial f}{\partial \mathbf{x}}(\mathbf{x}^*(t), \mathbf{u}^*(t)), \\ B(t) &= \frac{\partial f}{\partial \mathbf{u}}(\mathbf{x}^*(t), \mathbf{u}^*(t)), \end{aligned} \quad (10)$$

where $f(\mathbf{x}, \mathbf{u})$ is the vector concatenation of the right hand side of Eqs. 5 — 8. Then the feedback control law is

$$\mathbf{u}(t) = \mathbf{u}_r(t) - R^{-1} B^T(t) P(t) [\mathbf{x}(t) - \mathbf{x}_r(t)], \quad (11)$$

where $P(t)$ is the solution to the differential algebraic Riccati equation,

$$dot{P}(t) = Q + A^T(t) P(t) + P(t) A(t) - P(t) B(t) R^{-1} B^T(t) P(t), \quad (12)$$

which is solved by requiring $P(t_f) = 0$ and integrating backwards through time. The feedback gains, $R^{-1} B^T(t) P(t)$, can be computed offline for varying nominal conditions, reducing the burden of online computation requirements. The controller then reduces to a state-feedback controller with time-varying gains. This algorithm continues to be developed as complete and more accurate aerodynamic databases are generated.

Appendix

MDAO Tool Descriptions

Parametric Geometry and Mesh Generation In this model the flap geometry is parameterized as illustrated in Fig. 20a and 20b. The length and width of the root, L_{root} and W_{root} , are fixed based on the mechanical requirements for the

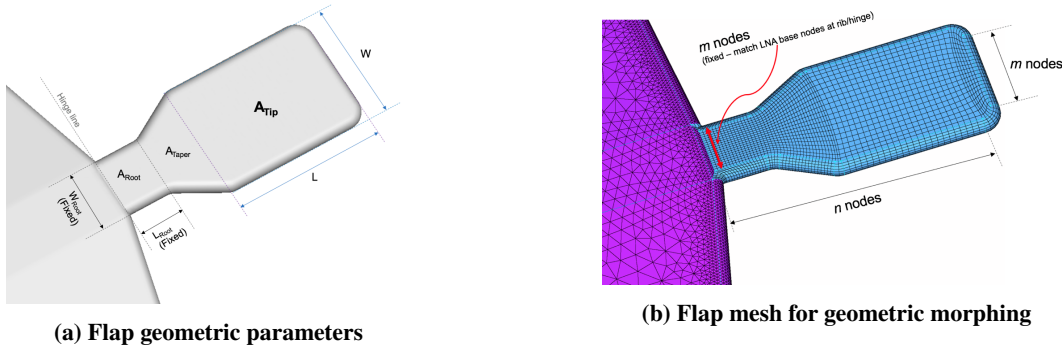


Fig. 20 Flap geometry parameterization and example of structured mesh morphing.

hinged flap mechanisms. This results in a fixed root area, A_{root} . The geometric parameters that can vary include the flap tip length (L), flap tip width (W), and the area of the tapered region (A_{taper}). These design variables directly affect the amount of flap area available for control. Each flap geometry is changed such that six of the eight tabs are the same size and two of the tabs are slightly smaller. Enabling automatic mesh generation of the tabs allows for downstream CFD solutions. A Delaunay triangulation routine could be used to produce these new surface triangulations. This parametric geometry and mesh generation routine is currently under development.

Configuration Based Aerodynamics (CBAero) with Anchoring CBAero [25] is a Modified Newtonian-based solver that provides rapid estimates of aerodynamic loads, moments, and surface heating. Databases, robustly generated with CBAero, provide initial aerodynamic estimates over a wide range of flight conditions and control surface configurations/deflections.

CBAero datasets are anchored to higher fidelity Computational Fluid Dynamics (CFD) solutions for increased accuracy. Aerodynamic forces and moments computed by these simulations are used in the development of the Control, Guidance, and Structural systems. Heating estimates are used in sizing the vehicle and control surface Thermal Protection System (TPS). Table 5 outlines the three CFD tools used in this analysis.

Table 5 CFD Software Utilized for LNA aerodynamic and aerothermodynamic simulations.

Software	Method	Provides
CBAero	Modified Newtonian	Engineering-level loads, moments, and surface estimates of aero & heating
Cart3D	Euler (Cartesian)	Inviscid loads, moments, surface estimates of aero, sonic effects, transonic/subsonic aft flow
US3D	Navier-Stokes (Non-equilibrium)	Pressure/viscous loads, moments, heating, sonic effects, transonic/subsonic aft flow, 6 DoF

Fidelity
↓

The first increased fidelity tool to be used is Cart3D, which is a Cartesian finite-volume inviscid CFD package. Cart3D captures flow phenomena including shocks and geometric influences and takes approximately 200 times more compute wall time than CBAero for a single solution. A run matrix may exceed one million cases for a given control surface configuration, making it intractable to use only Cart3D in the MDAO process. Accordingly, CBAero is used for the bulk of the aerodynamic database generation within the MDAO framework for control surface design and optimization. Higher fidelity solutions, for select flow conditions along the vehicle trajectory, are computed by anchoring the Cart3D results to the CBAero database. As the project progresses, US3D will be used to similarly anchor the aerodynamic and heating data to Navier-Stokes non-equilibrium CFD solutions. Anchoring does not require integrating Cart3D and US3D into the MDAO process, but allows for a set of correction factors to be applied to the CBAero database.

JSC Flight Analysis and Simulation Tool with Monte Carlo Assessing the size of the target footprint requires a vehicle flight dynamics model that allows for the development and integration of guidance and control algorithms. The MDAO framework will use NASA Johnson Space Center's Flight Analysis and Simulation Tool (FAST) to provide a 3DOF/6DOF vehicle flight dynamics simulation environment. The FAST architecture currently has several guidance and control algorithms available. This work will leverage the Fully Numerical Predictor-corrector Entry Guidance (FNPEG, [20]) algorithm to develop a direct force guidance control method (α , β modulation). Additionally, a robust modern control method, Linear Quadratic Regulator, will identify the needed flap commands to generate and track guidance commands.

Mass Estimating Relationships (MERs) MERs are under development for key control system components to enable the MDAO framework to vary component sizes, update component masses accordingly, and determine the final mass of the control system configuration. The variables for the flap MERs include flap size, structural/mechanism mass required to support maximum flap loads, motor size required to actuate a given flap size, battery mass required to power the actuators, and TPS mass required to protect the flaps from the thermal environment during entry. Various engineering tools will be used to establish an initial thermal-structural flap design which can feasibly accomplish the mission. These tools include MSC Nastran to ensure positive margins of safety for potential structural failure modes by various load cases from the life cycle of the trim tab control system. Additionally, TPSSizer and FIAT, programs used by the NASA-Ames Entry Systems Division [26] will be used to determine the amount of TPS mass required to protect the tabs from the heating predicted by CFD-based aeroheating analysis. The MERs will be developed based on at least

three designs in the trade space: 1) minimum flap size, 2) mid-size flap, and 3) maximum flap size. Currently, the maximum flap size is being used to build the NASTRAN and CBTPS simulations to develop the MERs.

Acknowledgments

The authors of this paper would like to thank NASA Space Technology Mission Directorate's Early Career Initiative (ECI) program for guiding and funding this work. Specifically, the ECI Program Executive Ricky Howard and our ECI Mentor Michelle Munk. We would also like to thank our collaborators in the Systems Analysis Office and the Entry Systems and Vehicle Development Branch at NASA Ames Research Center: Jeff Bowles, Dave Kinney, Kathy McGuire, Joseph Garcia, and Paul Wercinski. Additionally, we thank our collaborators in the Flight Mechanics & Trajectory Design Branch at NASA Johnson Space Center: Ron Sostaric, John Carson, Chris Cerimele, and Dan Matz. Finally, we thank our academic partner, the Human, Robotic, Vehicle Integration and Performance Laboratory at the University of California at Davis: Dr. Steve Robinson and graduate students.

References

- [1] Steinfeldt, B. A., Theisinger, J. E., Korzun, A. M., Clark, I. G., Grant, M. J., and Braun, R. D., "High Mass Mars Entry, Descent, and Landing Architecture Assessment," *AIAA Space 2009 Conference & Exposition*, AIAA 2009-6684, Pasadena, CA, 2009.
- [2] Cassell, A., Smith, B., Wercinski, P., Ghassemieh, S., Hibbard, K., Nelessen, A., and Cutts, J., "ADEPT, A Mechanically Deployable Re-Entry Vehicle System, Enabling Interplanetary CubeSat and Small Satellite Missions," *32nd Annual AIAA/USU Conference on Small Satellites*, SSC18-XII-18, Utah, 2018.
- [3] NASA/Space Technology Mission Directorate, "Adaptable, Deployable, Entry, and Placement Technology (ADEPT SR-1)," , 2018. URL <https://gameon.nasa.gov/adept-sr-1/>, date: 23.01.2018.
- [4] NASA/Space Technology Mission Directorate, "Hypersonic Inflatable Aerodynamic Decelerator," , 2014. URL https://www.nasa.gov/directories/spacetech/game_changing_development/HIAD/index.html, date: 05.06.2014.
- [5] D'Souza, S. N., and Sarigul-Klijn, N., "Survey of Planetary Entry Guidance Algorithms," *Journal of Progress in Aerospace Sciences*, Vol. 68, 2014, pp. 64–74.
- [6] NASA/Space Technology Mission Directorate, "Center Innovation Fund 2014 Winners Guidance and Control Architecture Design and Demonstration for Low Ballistic Coefficient Atmospheric Entry CIF," , 2014. URL <https://www.nasa.gov/centers/ames/cct/office/cif/2014-winners>.
- [7] NASA/Space Technology Mission Directorate, "Center Innovation Fund 2016 Winners Nano-ADEPT Lifting: Design Development for a Lifting Flight Test Demonstration," , 2016. URL <https://www.nasa.gov/centers/ames/cct/office/cif/p-Wercinski>.
- [8] Cianciolo, A. M., Davis, J. L., Engelund, W., Komar, D. R., and Queen, E., "Entry, Descent, and Landing Systems Analysis Study: Phase 2 Report on Exploration Feed-Forward Systems," *NASA Technical Manual*, , No. 217055, February 2011.
- [9] Cianciolo, A. M., and Polsgrove, T. T., "Human Mars Entry, Descent, and Landing Architecture Study Overview," *AIAA Space 2016*, AIAA 2016-5494, Long Beach, CA, 2016.
- [10] Korzun, A. M., Murphy, K. J., and Edquist, K. T., "Supersonic Aerodynamic Characteristics of Blunt Body Trim Tab Configurations," *31st AIAA Applied Aerodynamics Conference, Fluid Dynamics and Co-located Conferences*, AIAA 2013-2809, San Diego, CA, 2013.
- [11] McGuire, M., Gage, P., Galloway, E., Huynh, L., Nguyen, J., Bowles, J., and Windhorst, R., "Trajectory and Thermal Protection System Design for Reusable Launch Vehicles," *10th AIAA/ISSMO Multidisciplinary Analysis and Optimization Conference*, AIAA 2004-4490, 2004.
- [12] Garcia, J., Brown, J., Kinney, D., Bowles, J., Jiang, X., Dupzyk, I., Huynh, L., and Lau, E., "Co-Optimization of Mid Lift to Drag Vehicle Concepts for Mars Atmospheric Entry," *10th AIAA/ASME Thermophysics Conference*, AIAA 2010-5052, Chicago, IL, 2010.
- [13] Venkatapathy, E., Hamm, K., Fernandez, I., Arnold, J., Kinney, D., Laub, B., Makino, A., McGuire, M., Peterson, K., Prabhu, D., Empey, D., Dupzyk, I., Huynh, L., Hajela, P., Gage, P., Howard, A., and Andrews, D., "Adaptive Deployable Entry and Placement Technology (ADEPT): A Feasibility Study for Human Missions to Mars," *21st AIAA Aerodynamic Decelerator Systems Technology Conference and Seminar*, AIAA 2011-2608, Dublin, Ireland, 2011.

- [14] Tindol, R., "NASA: Genesis Sample Return," *Press Kit*, September 2004.
- [15] Serrano-Martinez, J., and Hechler, M., "Aerocapture guidance and navigation for the Rosetta Comet Nucleus Sample Return Mission," *Guidance, Navigation, and Control and Co-located Conferences*, AIAA 89-3381, 1989.
- [16] Ceglia, E., *European Users Guide to Low Gravity Platforms, Chapter 6*, European Space Agency, 2005.
- [17] Mitcheltree, R., Kellas, S., Dorsey, J., Desai, P., and Martin, C., "A passive Earth-entry capsule for Mars Sample Return," *7th AIAA/ASME Joint Thermophysics and Heat Transfer Conference*, AIAA 98-2851, 1998.
- [18] Gooding, J. L., "Scientific Guidelines for Preservation of Samples Collected from Mars," *NASA Technical Memorandum*, , No. 4148, April 1990.
- [19] Veverka, J., "Cryogenic Comet Nucleus Sample Return (CNSR) Mission Technology Study," *NASA SDO Report*, 2010.
- [20] Johnson, B. J., Cerimele, C. J., Stachowiak, S., Sostaric, R. R., Matz, D. A., and Lu, P., *Mid-Lift-to-Drag Ratio Rigid Vehicle Control System Design and Simulation for Human Mars Entry*, 2018.
- [21] de Boor, C., *Multivariate adaptive regression splines*, a practical guide to splines ed., Springer, 1978.
- [22] Ryschkewitsch, M. G., "Structural design and test factors of safety for spaceflight hardware," *NASA Technical Standard*, , No. NASA-STD-5001A, August 2008.
- [23] NASA Ames Research Center/Entry Systems and Technology Division, "Thermal Protection Material Branch," , 2018. URL <https://www.nasa.gov/content/thermal-protection-materials-branch>.
- [24] Kirk, D. E., *Optimal control theory: an introduction*, Prentice Hall, New Jersey, 1970.
- [25] Kinney, D., Garcia, J., and Huynh, L., "Predicted Convective and Radiative Aerothermodynamic Environments for Various Reentry Vehicles Using CBAERO," *AIAA Aerospace Sciences Meeting and Exhibit*, AIAA 2006-659, Reno, NV, 2006.
- [26] McGuire, M. K., Bowles, J., Yang, L., Kinney, D., and Roberts, C., "TPS Selection and Sizing Tool Implemented in an Advanced Engineering Environment," *42nd AIAA Aerospace Sciences Meeting and Exhibit*, AIAA 2004-342, 2004.